

Topological transitions induced by antiferromagnetism in a thin-film topological insulator

Qing Lin He^{*†,1} Gen Yin,^{1,*} Luyan Yu,^{1,*} Alexander J. Grutter,² Lei Pan,¹ Xufeng Kou,^{3,†}
Xiaoyu Che,¹ Guoqiang Yu,¹ Tianxiao Nie,¹ Bin Zhang,⁴ Qiming Shao,¹ Koichi Murata,¹
Xiaodan Zhu,¹ Yabin Fan,¹ Xiaodong Han,⁴ Brian J. Kirby,² and Kang L. Wang^{1,†}

¹*Department of Electrical Engineering,
University of California, Los Angeles, California 90095, USA.*

²*NIST Center for Neutron Research,
National Institute of Standards and Technology,
Gaithersburg, MD 20899-6102, USA.*

³*School of Information Science and Technology,
ShanghaiTech University, Shanghai 200031, China.*

⁴*Beijing Key Lab of Microstructure and Property of Advanced Materials,
Beijing University of Technology, 100124, Beijing, China.*

Abstract

Ferromagnetism in topological insulators (TIs) opens a topologically non-trivial exchange band gap, providing an exciting platform to manipulate the topological order through an external magnetic field. Here, we experimentally show that the surface of an antiferromagnetic thin film can independently control the topological order of the top and the bottom surface states of a TI thin film through proximity couplings. During the magnetization reversal in a field scan, two intermediate spin configurations stem from unsynchronized magnetic switchings of the top and the bottom AFM/TI interfaces. These magnetic configurations are shown to result in new topological phases with non-zero Chern numbers for each surface, introducing two counter-propagating chiral edge modes inside the exchange gap. This change in the number of transport channels, as the result of the topological transitions, induces antisymmetric magneto-resistance spikes during the magnetization reversal. With the high Néel ordering temperature provided by the antiferromagnetic layers, the signature of the induced topological transition persists in transport measurements up to a temperature of around 90 K, a factor of three over the Curie temperature in a typical magnetically doped TI thin film.

*These authors contributed to this work equally.

†Correspondence to: qlhe@ucla.edu; kouxf@shanghaitech.edu.cn; wang@ee.ucla.edu.

Currently there is immense interest in the manipulation of ferromagnetic phases in topological insulators (TIs) through either doping with magnetic species or through proximity coupling to a strong ferromagnetic system. This interest is driven by the novel physics which is predicted to emerge as a consequence of the TIs' non-trivial topology in k space [1–3]. The Dirac fermion surface states of three-dimensional TIs are robust against lattice defect perturbations, non-magnetic imperfections, and surface reconstructions [4–8]. Breaking time-reversal symmetry in these systems with magnetic dopants such as Cr or V opens an exchange band gap, inducing a finite Berry curvature and leading to an intrinsic anomalous Hall effect (AHE) [9, 10]. Inside this exchange gap, non-zero Chern numbers of ± 1 arise, protecting a chiral AHE edge mode which encircles the boundary of the TI thin film [1–3, 11]. Similar to the edge mode in conventional quantum Hall effects, back scattering is forbidden in the chiral mode, enabling dissipationless charge transport. Furthermore, the direction of the momentum and spin of the surface Dirac fermions are locked to be perpendicular, leading to many potential spintronic applications [12, 13]. These unique features make TIs a distinctive and exciting platform for investigating the interplay between charge and spin in topologically non-trivial matters.

Despite their exotic magneto-transport properties, the implementation of novel spintronic devices based on TI systems remain conceptual, largely due to the low magnetic ordering temperatures, small exchange gaps, and the potential fluctuations induced by the randomly distributed dopants. In search for high-temperature TI spintronics, conventional mechanisms to introduce ferromagnetic order suffer from significant limitations. For example, although higher Cr and V-doping levels increase the magnitude of the exchange gap, they also modify the band order such that the topologically protected surface states may be eliminated in heavily doped magnetic TIs [14–16]. This confinement to low-level doping restricts accessible Curie temperatures (T_C) to cryogenic temperatures, as the large distance between magnetic dopants weakens the Heisenberg exchange coupling between neighbouring spins. The other common method for achieving ferromagnetic TIs is interfacial proximity coupling to adjacent ferromagnets. Since the magnetic order in this case is introduced extrinsically by an adjacent ferromagnetic layer with a high T_C , it may persist at much higher temperatures than that induced by magnetic doping [17–19]. Proximity induced magnetization of the TI in these systems is both hard to achieve and extremely difficult to characterize, with the signal from the ferromagnet swamping out the contribution from the TI layers. Furthermore,

the ferromagnet produces significant stray fields and is easily affected by perturbations in external magnetic fields or currents, making crosstalk a problem, adversely affecting the device scalability [20].

Here, we propose the use of an antiferromagnet (AFM) interfacing to a TI thin film as an alternative method to introduce a higher- T_C magnetic order. Similar to the ferromagnet/TI system, the proximity-induced magnetization in the AFM/TI structure originates in the localized electronic wave-function overlap at the interface owing to the magnetically uncompensated surface of the AFM [21]. More importantly, proximity to AFMs has been experimentally shown to enhance the surface magnetization of a TI thin film induced by the interfacial exchange coupling [22]. AFMs have vanishingly small net magnetization and consequently neither produce stray fields nor affect the characterization of the TI layer. Therefore the magnetic order is robust against the external magnetic field or moderate current perturbations, minimizing the crosstalk between devices and improving scalability. Further, the precession of one spin sub-lattice in an AFM experiences a comparatively large effective field via the Heisenberg exchange coupling to the other spin sub-lattice [23]. Consequently, AFM spintronic devices can reach operating frequencies in the THz range, much higher than the GHz range accessible in ferromagnet-based devices [20, 24]. In this letter, we experimentally demonstrate the proximity-induced ferromagnetism at the AFM/TI [CrSb/(Bi,Sb)₂Te₃] interface in an AFM/TI bilayer, an AFM/TI/AFM trilayer, and an [AFM/TI]_n superlattice system. The uncompensated local spins at the interface magnetize the surface Dirac fermions in the TI robustly, giving rise to an observed AHE that survives up to 90 K, beyond the T_C of a typical magnetically doped TI of ~ 30 K. Equally important, we observed that the magnetizations of the top and the bottom TI surfaces can switch in a step-by-step manner. As a result, two antisymmetric magnetoresistance (MR) peaks show up during the sweep of the magnetic field. These two peaks correspond to different configurations in the spin texture, representing two distinct topological orders.

Firstly, in order to ascertain the magnetic order in CrSb thin films, superconducting quantum interference device magnetometry (SQUID) and magneto-transport measurements were carried out on a 12 nm CrSb layer grown on a GaAs substrate. An external magnetic field was applied perpendicularly to the film plane. As shown in Fig. 1a, a vanishingly weak magnetization is captured in the M-H measurement, diminishing quickly as the temperature increases to ~ 20 K. Such a small magnetization is likely to originate

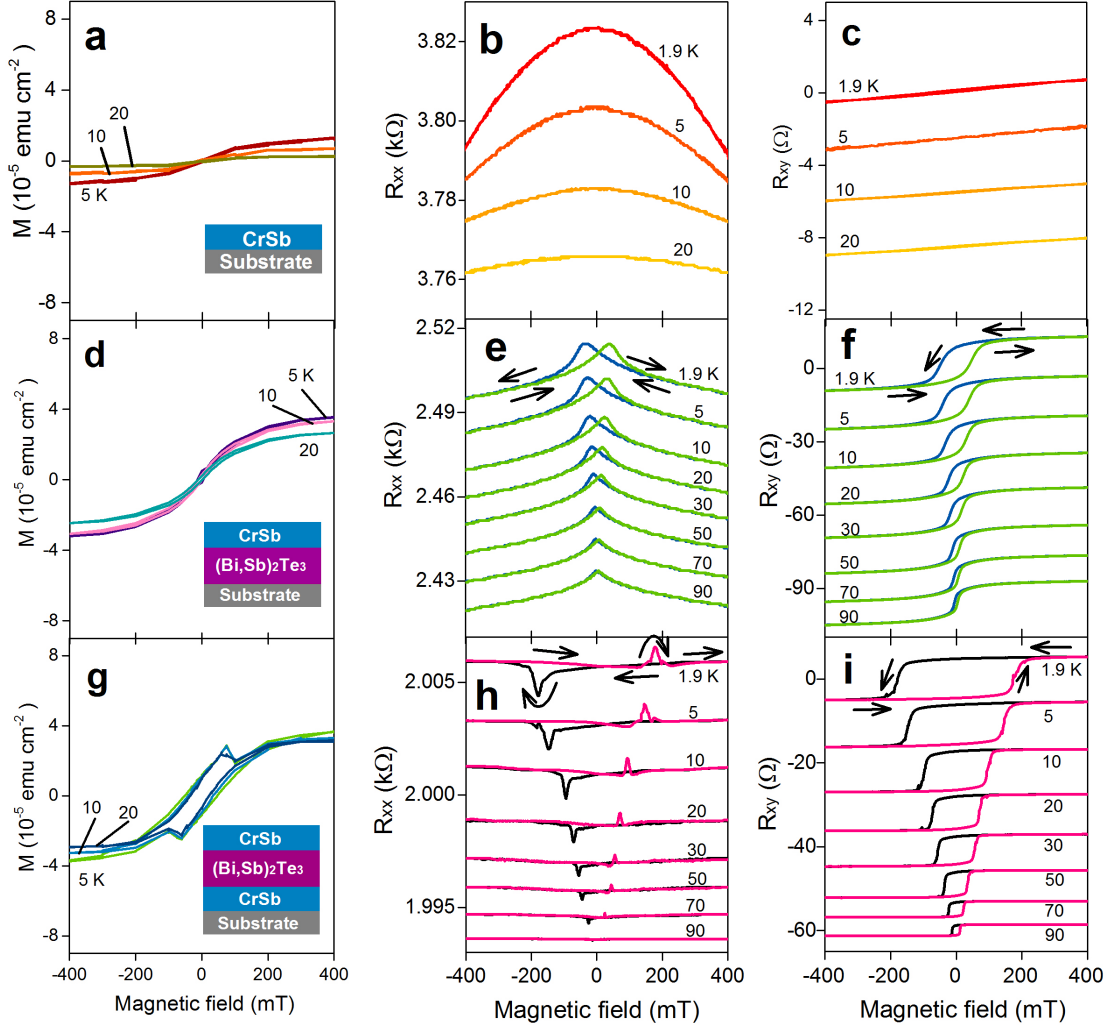


Figure 1: Emerging surface magnetizations in antiferromagnet/topological insulator (AFM/TI) structures. **a**, temperature-dependent M-H loops of a 12-nm AFM thin film, CrSb, grown on a GaAs substrate, which exhibits negligible magnetization. **b** and **c** show the results of the longitudinal (R_{xx}) and the Hall (R_{xy}) resistance, respectively. The absence of hysteresis in both measurement results, i.e. the small parabolic curvature in R_{xx} and the linear response in R_{xy} , suggest that the CrSb layer does not generate an AHE intrinsically. **d-f** show the corresponding results of an AFM/TI bilayer, demonstrating the transport signature of the top-surface magnetization of the TI layer induced by proximity. **g-i** are from an AFM/TI/AFM trilayer, in which an antisymmetric MR behavior and an AHE are observed. Compared with the bilayer case, the trilayer contains two individually magnetized TI surfaces due to the proximity to two CrSb layers, respectively. This allows an intermediate topological order of the TI thin film when the top and bottom TI surfaces switch in a step-by-step manner. ($1 \mu\text{emu} = 1 \text{ nA} \cdot \text{m}^2$)

from the uncompensated spins in the AFM layer at the interface [21, 22]. Consistently, magneto-transport measurements also capture a small negative MR which also vanishes at around 20 K (Fig. 1b). The corresponding Hall resistance obtained (Fig. 1c) in a $2\text{ mm} \times 1\text{ mm}$ Hall bar varies linearly with the external field, indicating that the Hall signal is mainly associated with the ordinary Hall effect. These results suggest that the weak magnetization in the CrSb thin film results in neither magnetic hysteresis nor intrinsic AHE.

Strikingly, when the AFM layer was epitaxially grown on a 8-nm TI thin film, a proximity-induced AHE was observed. As shown in Fig. 1d, the saturation magnetization is roughly $4 \times 10^{-5} \text{ emu} \cdot \text{cm}^{-2}$, which is higher than that of the single AFM layer grown on the substrate (Fig. 1a). This indicates that the polarized TI surface spins contribute extra magnetic moments to the saturated magnetization. Furthermore, the MR measurement exhibits a hysteretic butterfly shape which gradually vanishes as the temperature increases to 90 K, as shown in Fig. 1e. The corresponding Hall resistance results are shown in Fig. 1f. In this figure, a significant AHE signal is evidenced by the large hysteresis even without subtracting the linear ordinary Hall resistance, indicating a strong magnetic proximity effect in the AFM/TI bilayer. Moreover, the observed AHE persists at 90 K, which is roughly a factor of three higher than the T_C of a typical Cr-doped TI. This enhancement in T_C implies that the AHE does not originate from Cr diffusion into the TI layer, but is rather dominated by a proximity-induced AHE, since an extremely heavy Cr doping concentration would be required to achieve such a high T_C . In such a heavily-doped case, the TI film would exhibit a strong perpendicular magnetization, sharply contradicted by the weak magnetic moment observed in the AFM/TI bilayer with SQUID, as shown in Fig. 1d.

Surprisingly, when introducing one additional AFM layer to produce a AFM/TI/AFM sandwich structure, another distinct magnetic feature is revealed. In contrast to Figs. 1a and d, the M-H results show clear hysteresis loops from 5 K to 20 K (Fig. 1g), which implies the presence of unsynchronized switching of the top and the bottom AFM layers, given that the interfacial exchange coupling experienced by the uncompensated spins is strongly determined by the details (e.g. roughness, defect density, etc.) at the interfaces. Corresponding to this double-switching, the temperature-dependent MR curves show antisymmetric spikes during the magnetization reversal process, as shown in Fig. 1h, and these spikes occur when the corresponding AHE resistance changes sign (Fig. 1i). Meanwhile, both the spike-to-spike

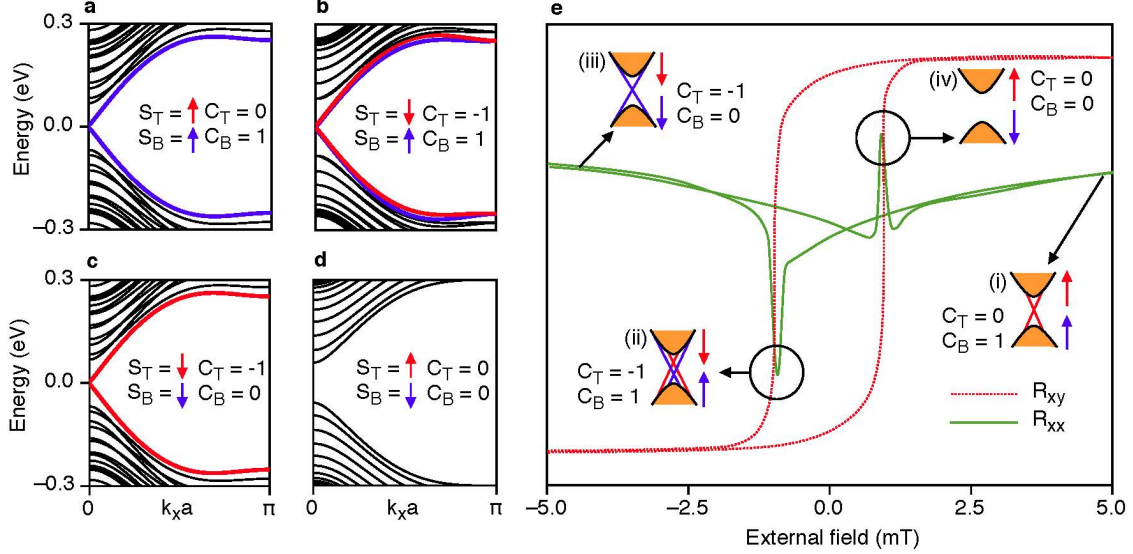


Figure 2: The topological transition during the double-switching magnetization reversal. **a-d**, The band structure of a TI thin film with different top-bottom (red-blue) spin configurations ($B = 16.45 \text{ eV}\tilde{v}_l\text{e}^{-2}$, $\gamma = 3.29 \text{ eV}\tilde{v}_l\text{e}^{-1}$, $J_H = 0.05 \text{ eV}$). A negligibly small top-bottom potential drop is numerically added to **b** for clarity. **e**, The topological transition during the reversal of the total magnetization as remarked near the AHE hysteresis and the corresponding MR curves. The four different topological orders (i-iv) and their band structures are also schematically shown at different transition points during the field scan. These four different cases (i-iv) correspond to the band structures as shown in **a-d**.

distance of the MR curve and the coercivity of the AHE loop have a temperature dependence which closely matches that of the AFM/TI case with a phase change temperature of around 90 K, underscoring the importance of the interfacial magnetic proximity effect induced by the two AFM layers. This antisymmetric MR contrasts sharply with the symmetric MR observed in most ferromagnetic systems [17], as well as the AFM/TI bilayer in this work. We note that all the M-H, MR, and AHE results presented in Fig. 1 are reproducible across different batches of samples/devices, enabling us to exclude experimental artifacts related to the device architectures (e.g. misalignment of the Hall voltage leads, device sizing effects, etc.). Consequently, we propose that the observed antisymmetric MR of the AFM/TI/AFM trilayer samples has a surprising origin - topological transitions induced by the double-switching mechanism, as discussed below.

In the AFM/TI/AFM trilayer, the TI layer can be described by the effective four-band

Hamiltonian [25]:

$$H_0 = \begin{pmatrix} -Bk^2 & i\gamma k_- & V & 0 \\ -i\gamma k_+ & Bk^2 & 0 & V \\ V & 0 & Bk^2 & i\gamma k_- \\ 0 & V & -i\gamma k_+ & -Bk^2 \end{pmatrix} + H_H \quad (1)$$

where $B > 0$ is the parabolic massive component induced by the surface-to-surface coupling, V denotes the structural inversion asymmetry due to the top-to-bottom electrostatic potential drop, and $\gamma = \hbar v_F$, where v_F is the constant group velocity of the surface Dirac fermions [26, 27]. Due to the surface magnetization, a Hund's-rule coupling term, H_H , is added to break the time-reversal symmetry:

$$H_H = -J_H \begin{pmatrix} \mathbf{S}_T \cdot \boldsymbol{\sigma} & 0 \\ 0 & \mathbf{S}_B \cdot \boldsymbol{\sigma} \end{pmatrix} \quad (2)$$

Here, \mathbf{S}_T and \mathbf{S}_B represent the spin configurations of the top and the bottom surface Dirac fermions under the influence of the AFM-induced proximity effect. J_H denotes the interfacial Hund's-rule coupling and in this case $J_H > 0$. In order to model the magneto-electric transport behavior of the trilayer structure, we establish a tight-binding model by discretizing $k_\alpha \rightarrow -i\partial_\alpha$. Usually applying a Dirac fermion Hamiltonian in a lattice structure introduces a Fermi doubling problem, such that the dispersion unphysically closes the gap at the boundary of the Brillouin zone [28, 29]. However, in the thin-film case, the non-zero surface-to-surface hybridization-induced parabolic term resolves this problem [30]. The band structure of a thin film with confined boundaries can be obtained using this tight binding model with different spin configurations, as shown in Figs. 2a-d. Note that H_H adds massive terms to the total Hamiltonian, such that the reversals of \mathbf{S}_T and \mathbf{S}_B change the band order, inducing topological transitions [31]. Assuming a negligible structural inversion asymmetry term, $V = 0$. Thus, the two surfaces are block-diagonalized such that the total Chern number is the sum of the Chern numbers given by the two surfaces: $C = C_T + C_B$. Unlike the case of a pure Dirac fermion, due to the surface-to-surface hybridization, a finite $B > 0$ in Eq. 1 makes the upper-left block a typical 2×2 Hamiltonian of the quantum AHE, where integer Chern numbers of ± 1 are introduced inside the exchange gap, rather than $\pm 1/2$ [25, 31]. As shown in Figs. 2a-d, the four different spin configurations correspond to different combinations of C_T and C_B . When \mathbf{S}_T and \mathbf{S}_B are parallel, integer total Chern

numbers are introduced: $C = \pm 1$ (Figs. 2a and c). In an ideal case where only the TI surface states contribute to the conduction, these two non-zero Chern number configurations give rise to the quantum AHE, where boundary modes of opposite chiralities are established with different saturation directions of the total magnetization. The dispersions of these modes are shown as the coloured linear bands in Figs. 2a and c.

During the reversal of the magnetization, unsynchronized switching occurs, inducing two intermediate spin configurations with different topological orders. On one hand, when $\mathbf{S}_T = \uparrow$ and $\mathbf{S}_B = \downarrow$, $C_T = C_B = 0$, and the magnetic exchange gap in the TI becomes trivial (Fig. 2d). On the other hand, in the case when $\mathbf{S}_T = \downarrow$ and $\mathbf{S}_B = \uparrow$, the non-trivial edge modes with two-fold degeneracy appear (i.e., $C_T = -1$ and $C_B = 1$, see Fig. 2b), yet the total Chern number is still $C = C_T + C_B = 0$. Accordingly, in both of the two configurations (Figs. 2b and d), the Hamiltonian in Eq. 1 restores its time-reversal symmetry, such that the total Berry curvature is zero and the intrinsic Hall signal is suppressed. However, since the number of modes inside the exchange gap changes by two, the MR changes significantly when the Fermi level (ϵ_F) is close to the Dirac point, leading to the antisymmetric R_{xx} behavior. In Fig. 2e, typical R_{xx} and R_{xy} of an AFM/TI/AFM trilayer are plotted together, where band structures with different topological orders are also illustrated at different stages of the magnetic field scan.

In order to numerically evaluate the longitudinal resistance, the transport behavior of a six-terminal Hall bar (as shown in Fig. 3a) is numerically evaluated using nonequilibrium Green's functions, based on the tight-binding Hamiltonian established from Eq. 1 (see Methods) [32, 33]. At zero temperature, the Hall resistance, R_{xy} , and the longitudinal resistance, R_{xx} as functions of ϵ_F are shown in Fig. 3b, corresponding to the case of $\mathbf{S}_T = \mathbf{S}_B = \uparrow$. A quantized plateau of R_{xy} and a zero R_{xx} are demonstrated when ϵ_F is within the exchange gap. The local density of states near the Dirac point of the Hall bar is shown as a colour contrast in Fig. 3a, where a single state of the chiral mode is localized at the boundaries. When $k_B T$ increases to $0.6J_H$, the thermal broadening begins to include sub-bands, such that the quantization of the AHE begins to vanish, namely, R_{xy} decreases while R_{xx} increases inside the exchange gap. In the experiment, the AHE does not reach the quantized level. This indicates that states outside the magnetic exchange band gap are involved in the transport due to either the thermal broadening or the band-edge fluctuations. In this calculation, $k_B T > J_H$ is applied to mimic this effect. R_{xx} at the four different spin

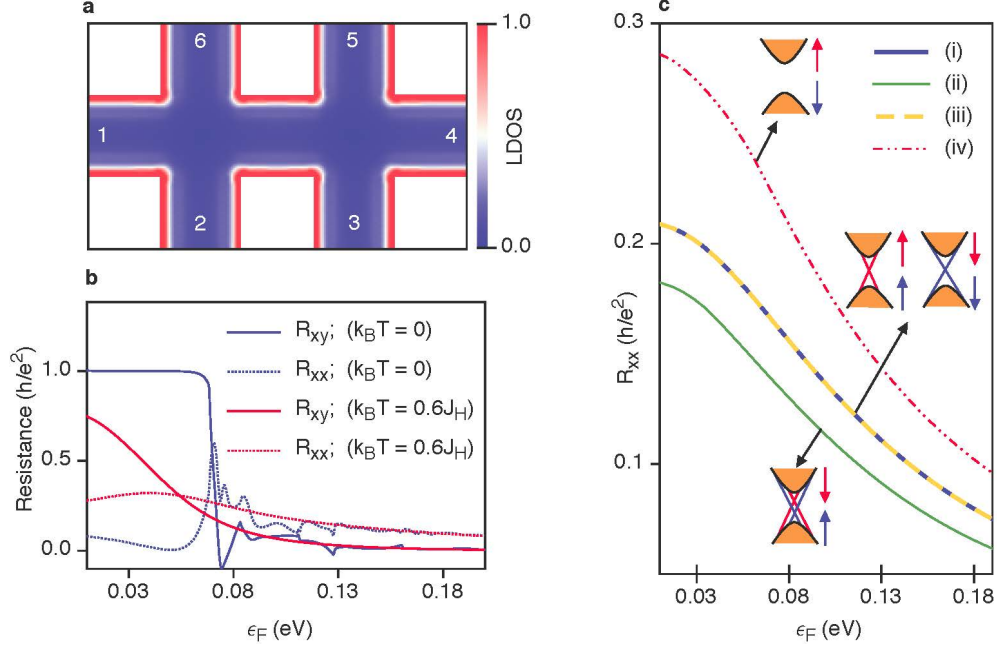


Figure 3: Numerical simulation results of the charge transport in the Hall bar. **a**, The device structure constructed by the tight-binding model corresponding to Eq. 1. Local density of states calculated at $\epsilon_F = 0.03$ eV is illustrated by the colour plot. **b**, R_{xy} and R_{xx} obtained from a nonequilibrium Green's function calculation at different temperatures. Longitudinal current is applied between terminal 1 and 4. R_{xy} is obtained from terminal 2 and 6, while R_{xx} is calculated between terminal 2 and 3. **c**, R_{xx} as a function of ϵ_F for the four different spin configurations ($k_B T = 1.4 J_H$). Details of the band structures corresponding to different topological orders (i-iv) are schematically shown for each case. Note that the yellow and blue lines coincide together.

configurations are shown in Fig. 3c, where (i), (ii), (iii) and (iv) correspond to the band structures in Figs. 2a-d, respectively. We found that the R_{xx} values of (i) and (iii) are higher than (ii) and lower than (iv) in this scenario, suggesting the R_{xx} of the two anti-parallel configurations of \mathbf{S}_T and \mathbf{S}_B , i.e. $(\mathbf{S}_T, \mathbf{S}_B) = (\uparrow, \downarrow)$ and $(\mathbf{S}_T, \mathbf{S}_B) = (\downarrow, \uparrow)$, are greater and smaller than the R_{xx} in the parallel cases, respectively. Thus, configuration (ii) produces a dip in R_{xx} , while configuration (iv) produces a peak (Fig. 2e).

Following the magnetization switching-related topological transition model described above, it is expected that the proximity-induced AHE and the antisymmetric MR features will become more pronounced in the $(\text{AFM}/\text{TI})_n$ (n is defined as the repeating number of the AFM/TI bilayer) superlattice structure where more non-identical AFM/TI interfaces

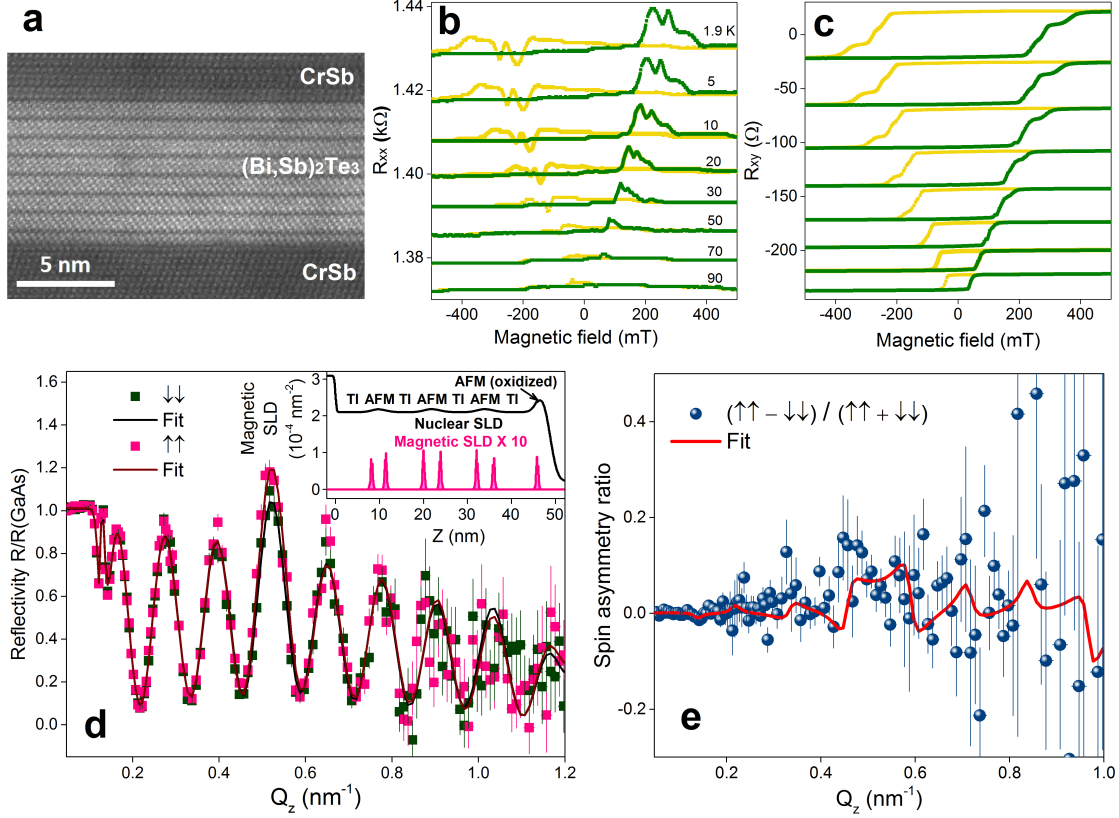


Figure 4: Multi-channel magnetic proximity effect in a $(\text{TI}/\text{AFM})_n$ superlattice (SL).

a, a cross-sectional scanning transmission electron microscope image obtained from a SL, which captures the sharp interfaces between the TI layer sandwiched by two AFM layers. There is a small in-plane rotation between the top and the bottom CrSb layers when interfacing with TI surfaces, i.e. the top AFM layer is taken along the $(\bar{1}2\bar{1}0)$ zone axis while the bottom one slightly deviates from it. **b** and **c**, R_{xx} and R_{xy} results of the superlattice as functions of external perpendicular magnetic fields at different temperatures. **d**, polarized neutron reflectivity and **e**, spin asymmetry (at 5 K with a 700 mT in-plane field) normalized to the GaAs substrate for the spin-polarized $R_{\uparrow\uparrow}$ and $R_{\downarrow\downarrow}$ channels of the SL. The inset in **d** shows the corresponding model with structural and magnetic scattering length densities (SLDs) used to obtain the best fit. The error bars are ± 1 standard deviation.

become involved in the proximity process. To confirm this scenario, we prepared a high-quality superlattice of $n = 4$ (Fig. 4a), and performed the temperature-dependent magneto-transport measurements. As expected, even stronger antisymmetric MR and AHE signals are present; furthermore, multiple spikes are observed in the MR loops during the

magnetization reversal, which again coincide with the multiple Hall-resistance steps near the coercivities. Similar to the AFM/TI/AFM trilayer case, these features likely indicate the unsynchronized switchings of different interfacial channels and the multiple-switching behavior may stem from larger variations in the switching fields due to the increased number of slightly different AFM/TI interfaces. Figs. 4b and c provide direct experimental evidences that the magnetization reversal process occurs in a step-by-step manner in such a superlattice structure.

To quantitatively investigate the net magnetic polarization with detailed depth-dependent information, we probed a representative $n = 4$ superlattice using polarized neutron reflectometry (PNR). PNR was performed at 5 K in an applied in-plane magnetic field of 700 mT, and the non spin-flip specular reflectivities, sensitive to the depth profile of the nuclear scattering length density and net in-plane magnetization, were measured as a function of the momentum transfer vector Q_Z . Fig. 4d shows the fitted reflectivities alongside the most likely nuclear and magnetic depth profile, while the magnetic features may be more clearly seen in the spin asymmetry ratio (defined as the difference between the two non spin-flip reflectivities normalized by their sum) plotted in Fig. 4e. In this figure, with the spin asymmetry, we observe small but nonzero splitting (a small dip) between the reflectivities near the critical edge ($Q_Z = 0.15 \text{ nm}^{-1}$) and at the first order superlattice reflection ($Q_Z = 0.4 - 0.6 \text{ nm}^{-1}$). Although the resulting magnetization is extremely weak, the statistical significance of the two features is three and six standard deviations, respectively.

In fitting the data, we find several models which may describe the data. The most plausible of these, shown in the inset of Fig. 4d, exhibits a net magnetization at the interfacial regime. In such a model, the interfacial TI possesses a net magnetization of approximately $30 \text{ emu} \cdot \text{cm}^{-3}$. We note that the PNR data can also be described quite well by alternative models as discussed in Supplementary Information. However, the model in which all of the magnetization is localized within the TI yield splitting at the superlattice peak which is the opposite sign of the measurement. Furthermore, confining all of the magnetization uniformly within the AFM layer cannot simultaneously match the splitting magnitude at the critical edge and superlattice peak. Finally, although a model assuming uniform non-zero magnetizations in both the TI and the AFM layers fits well, there is no clear mechanism by which the bulk TI might become ferromagnetic through the entire layer.

Therefore, all of these alternative models (Models 1-3 in Supplementary Information) are eliminated from consideration and we conclude that a modulated magnetic depth profile must be present, with the magnetization mainly distributed at the interfaces. This is consistent with the observed proximity-induced magnetizations at the AFM/TI interfaces in both the bilayer and trilayer structures.

In summary, we have experimentally demonstrated transport signatures which indicate a topological transition induced by the anti-parallel magnetizations of the top and the bottom surface states in a TI thin film. The emergent surface magnetization of a TI is induced through proximity coupling to antiferromagnetic layers. When both surfaces are magnetized, two intermediate spin configurations, i.e., $(\mathbf{S}_T, \mathbf{S}_B) = (\uparrow, \downarrow)$ and $(\mathbf{S}_T, \mathbf{S}_B) = (\downarrow, \uparrow)$, are introduced during the magnetization reversal process. These intermediate states restore the overall time-reversal symmetry of the two-surface system. One of the two intermediate states, i.e. $(\mathbf{S}_T, \mathbf{S}_B) = (\downarrow, \uparrow)$, introduces a set of two Chern numbers of ± 1 , resulting in two counter-propagating chiral edge modes inside the exchange gap. This change in the number of transport channels induces antisymmetric magnetoresistance spikes during the scan of the external field, which exactly coincide with the coercive field of the AHE. By growing an $(\text{AFM}/\text{TI})_{n=4}$ superlattice, we introduce more AFM/TI interfaces with different spin configurations, and can more clearly demonstrate the switching-related topological transition as well as enhance the AFM-induced proximity effect. This AFM-TI structure provides a promising new framework for the manipulation of topological orders in TI thin films.

Methods

A. Film growth

All the films were fabricated using an ultrahigh vacuum molecular beam epitaxy system. Semi-insulating (resistivity larger than $10^6 \Omega\text{-cm}$) GaAs (111) substrates were pre-annealed in the growth chamber at 580 °C for the desorption of the native surface oxide. The substrate temperature was then reduced and maintained at 200 °C for the remainder of the fabrication process. High-purity Bi and Cr were evaporated from standard Knudsen cells while Sb and Te were evaporated by standard thermal cracker cells. All the epitaxial growth was monitored by an in-situ reflection high-energy electron diffraction (RHEED).

For the growth of both $(\text{Bi,Sb})_2\text{Te}_3$ and CrSb layers, the growth conditions were optimized to obtain very sharp, smooth, streaky RHEED patterns, while the intensity oscillations were used to calibrate growth rates. These growth rates were determined to be around 0.08 and 0.06 Å/s for $(\text{Bi,Sb})_2\text{Te}_3$ and CrSb, respectively. After growth, 2 nm of Al layers were evaporated on all the sample surfaces in-situ at room temperature for protection against contamination and oxidation.

B. Nonequilibrium Green's function calculation

The NEGF calculation was carried out using the tight-binding model established from the $k \cdot p$ Hamiltonian (Eq. 1) by discretizing the differential operators after applying $k_\alpha \rightarrow -i\partial_\alpha$. The terminals were assumed to be semi-infinite leads which were truncated into self-energy terms: $\mathbf{G}^R = [\epsilon - \mathbf{H}_D - \sum_i \boldsymbol{\Sigma}_i]^{-1}$, where \mathbf{G}^R is the retarded Green's function, \mathbf{H}_D is the isolated tight-binding Hamiltonian of the device, and $\boldsymbol{\Sigma}_i = \mathbf{t}_i^\dagger \mathbf{g}_i^R \mathbf{t}_i$ is the self energy obtained from the surface Green's function (\mathbf{g}_i^R) and the hopping term between the device and the semi-infinite leads (\mathbf{t}_i). Following the standard Landauer-Büttiker linear response picture, the terminal current, I_i , and the voltage, $V_i = \mu_i/e$, can be obtained from $\mathbf{I} = \frac{e}{h} [\int (-\frac{\partial f_0}{\partial \epsilon}) \mathbf{T}(\epsilon) d\epsilon] \delta\boldsymbol{\mu}$, where $f_0(\epsilon - \epsilon_F)$ is the Fermi distribution, $\mathbf{I} = (I_1, I_2, \dots, I_6)^T$ denotes the current at different terminals, and $\delta\boldsymbol{\mu} = (\delta\mu_1, \dots, \delta\mu_6)^T$ is the chemical potential shift ($\delta\mu_i = \mu_i - \epsilon_F$). The transmission matrix was obtained by $T_{i,j} = \text{Tr}[\boldsymbol{\Gamma}_i \mathbf{G}_{i,j}^R \boldsymbol{\Gamma}_j \mathbf{G}_{i,j}^A]$ for $i \neq j$ and $T_{i,i} = -\sum_{j \neq i} T_{i,j}$, where $\boldsymbol{\Gamma}_i = i(\boldsymbol{\Sigma}_i - \boldsymbol{\Sigma}_i^\dagger)$ and $\mathbf{G}_{i,j}^A = \mathbf{G}_{i,j}^{R\dagger}$. The Hall resistance can be obtained by fixing the bias along the longitudinal direction and solving for the bias at different terminals, assuming zero terminal currents in the transverse direction.

C. Polarized Neutron Reflectometry

PNR measurements were performed using the polarized beam reflectometer (PBR) instrument at the NIST Center for Neutron Research. The sample was cooled to 5 K in an applied in-plane field of 700 mT. Incident and scattered neutrons were spin polarized either spin-up (\uparrow) or spin-down (\downarrow) with respect to the applied magnetic field. Two spin-flippers and polarizing supermirrors were used to select the incident and scattered neutron polarization

direction. Thus, we measured the non spin-flip reflectivities as a function of the momentum transfer along the film normal direction in a range of $0.1 \sim 1.0 \text{ nm}^{-1}$. The neutron propagation direction was perpendicular to both the sample surface and the applied field direction. Based on magnetometry measurements showing in-plane magnetization saturation below the applied field of 700 mT, spin-flip scattering is not expected. Therefore, we measured the spin-up and spin-down reflectivities using full polarization analysis to ensure that the incident and scattered beams retained identical neutron polarization directions. We refer, therefore, only to the spin-up and spin-down non-spin-flip reflectivities, which are functions of the nuclear and magnetic scattering length density profiles. The magnetic profile was deduced through modeling of the data with the NIST Refl1D software package.

Acknowledgments

The transport measurement and the theoretical modeling in this work are supported by the Spins and Heat in Nanoscale Electronic Systems (SHINES), an Energy Frontier Research Center funded by the US Department of Energy (DOE), Office of Science, Basic Energy Sciences (BES) under award #SC0012670. We are also grateful to the support from the National Science Foundation (DMR-1411085), and the ARO program under contract W911NF-15-1-10561. We also acknowledge the support from the FAME Center, one of six centres of STARnet, a Semiconductor Research Corporation program sponsored by MARCO and DARPA. Certain commercial equipment, instruments, or materials are identified in this paper to foster understanding. Such identification does not imply recommendation or endorsement by the National Institute of Standards and Technology, nor does it imply that the materials or equipment identified are necessarily the best available for the purpose.

-
- [1] C.-Z. Chang, J. Zhang, X. Feng, J. Shen, Z. Zhang, M. Guo, K. Li, Y. Ou, P. Wei, L.-L. Wang, et al., *Science* **340**, 167 (2013), ISSN 0036-8075, 1095-9203.
 - [2] X. Kou, S.-T. Guo, Y. Fan, L. Pan, M. Lang, Y. Jiang, Q. Shao, T. Nie, K. Murata, J. Tang, et al., *Phys. Rev. Lett.* **113**, 137201 (2014).
 - [3] R. Yu, W. Zhang, H.-J. Zhang, S.-C. Zhang, X. Dai, and Z. Fang, *Science* **329**, 61 (2010), ISSN 0036-8075, 1095-9203.

- [4] X.-L. Qi and S.-C. Zhang, *Rev. Mod. Phys.* **83**, 1057 (2011).
- [5] M. Z. Hasan and C. L. Kane, *Rev. Mod. Phys.* **82**, 3045 (2010).
- [6] C. L. Kane and E. J. Mele, *Phys. Rev. Lett.* **95**, 146802 (2005).
- [7] H. Zhang, C.-X. Liu, X.-L. Qi, X. Dai, Z. Fang, and S.-C. Zhang, *Nat Phys* **5**, 438 (2009), ISSN 1745-2473.
- [8] B. A. Bernevig, T. L. Hughes, and S.-C. Zhang, *Science* **314**, 1757 (2006), ISSN 0036-8075, 1095-9203.
- [9] N. Nagaosa, J. Sinova, S. Onoda, A. H. MacDonald, and N. P. Ong, *Rev. Mod. Phys.* **82**, 1539 (2010).
- [10] D. Xiao, M.-C. Chang, and Q. Niu, *Rev. Mod. Phys.* **82**, 1959 (2010).
- [11] C.-Z. Chang, W. Zhao, D. Y. Kim, H. Zhang, B. A. Assaf, D. Heiman, S.-C. Zhang, C. Liu, M. H. W. Chan, and J. S. Moodera, *Nat Mater* **14**, 473 (2015), ISSN 1476-1122.
- [12] Y. Fan, P. Upadhyaya, X. Kou, M. Lang, S. Takei, Z. Wang, J. Tang, L. He, L.-T. Chang, M. Montazeri, et al., *Nat Mater* **13**, 699 (2014), ISSN 1476-1122.
- [13] A. R. Melnik, J. S. Lee, A. Richardella, J. L. Grab, P. J. Mintun, M. H. Fischer, A. Vaezi, A. Manchon, E.-A. Kim, N. Samarth, et al., *Nature* **511**, 449 (2014), ISSN 0028-0836.
- [14] X. F. Kou, W. J. Jiang, M. R. Lang, F. X. Xiu, L. He, Y. Wang, Y. Wang, X. X. Yu, A. V. Fedorov, P. Zhang, et al., *Journal of Applied Physics* **112**, 063912 (2012), ISSN 0021-8979, 1089-7550.
- [15] J. Zhang, C.-Z. Chang, P. Tang, Z. Zhang, X. Feng, K. Li, L.-l. Wang, X. Chen, C. Liu, W. Duan, et al., *Science* **339**, 1582 (2013), ISSN 0036-8075, 1095-9203.
- [16] Y. Jiang, C. Song, Z. Li, M. Chen, R. L. Greene, K. He, L. Wang, X. Chen, X. Ma, and Q.-K. Xue, *Phys. Rev. B* **92**, 195418 (2015).
- [17] M. Lang, M. Montazeri, M. C. Onbasli, X. Kou, Y. Fan, P. Upadhyaya, K. Yao, F. Liu, Y. Jiang, W. Jiang, et al., *Nano Lett.* **14**, 3459 (2014), ISSN 1530-6984.
- [18] Z. Jiang, C.-Z. Chang, C. Tang, P. Wei, J. S. Moodera, and J. Shi, *Nano Lett.* **15**, 5835 (2015), ISSN 1530-6984.
- [19] F. Katmis, V. Lauter, F. S. Nogueira, B. A. Assaf, M. E. Jamer, P. Wei, B. Satpati, J. W. Freeland, I. Eremin, D. Heiman, et al., *Nature* **533**, 513 (2016), ISSN 0028-0836.
- [20] T. Jungwirth, X. Marti, P. Wadley, and J. Wunderlich, *Nat Nano* **11**, 231 (2016), ISSN 1748-3387.

- [21] W. Luo and X.-L. Qi, Phys. Rev. B **87**, 085431 (2013).
- [22] Q. L. He, X. Kou, A. J. Grutter, G. Yin, L. Pan, X. Che, Y. Liu, T. Nie, B. Zhang, S. M. Disseler, et al., Nat Mater **advance online publication** (2016), ISSN 1476-1122.
- [23] F. Keffer and C. Kittel, Phys. Rev. **85**, 329 (1952).
- [24] R. Cheng, D. Xiao, and A. Brataas, Phys. Rev. Lett. **116**, 207603 (2016).
- [25] W.-Y. Shan, H.-Z. Lu, and S.-Q. Shen, New J. Phys. **12**, 043048 (2010), ISSN 1367-2630.
- [26] H.-Z. Lu, A. Zhao, and S.-Q. Shen, Phys. Rev. Lett. **111**, 146802 (2013).
- [27] H.-Z. Lu, W.-Y. Shan, W. Yao, Q. Niu, and S.-Q. Shen, Phys. Rev. B **81**, 115407 (2010).
- [28] R. Stacey, Phys. Rev. D **26**, 468 (1982).
- [29] L. Susskind, Phys. Rev. D **16**, 3031 (1977).
- [30] K. M. M. Habib, R. N. Sajjad, and A. W. Ghosh, Applied Physics Letters **108**, 113105 (2016), ISSN 0003-6951, 1077-3118.
- [31] X.-L. Qi, T. L. Hughes, and S.-C. Zhang, Phys. Rev. B **82**, 184516 (2010).
- [32] S. Datta, *Quantum Transport: Atom to Transistor* (Cambridge University Press, Cambridge, UK ; New York, 2005), 2nd ed., ISBN 9780521631457.
- [33] R. Lake, G. Klimeck, R. C. Bowen, and D. Jovanovic, Journal of Applied Physics **81**, 7845 (1997), ISSN 0021-8979, 1089-7550.